Check for updates

View Article Online
View Journal

Journal of
Materials Chemistry A
Materials for energy and sustainability

Accepted Manuscript

This article can be cited before page numbers have been issued, to do this please use: S. Chen, T. Han, J. Liu, X. Liang, J. Yang and B. Z. Tang, *J. Mater. Chem. A*, 2022, DOI: 10.1039/D2TA02918A.

Volume 6
Number 12
28 March 2018
Pages 4883-5230

Journal of
Materials Chemistry A
Materials for energy and sustainability
rsc.li/materials-a

ISSN 2050-7488

ROYAL SOCIETY
OF CHEMISTRY

COMMUNICATION
Zhenhai Wen *et al.*
An electrochemically neutralized energy-assisted low-cost acid-alkaline electrolyzer for energy-saving electrolysis hydrogen generation

This is an Accepted Manuscript, which has been through the Royal Society of Chemistry peer review process and has been accepted for publication.

Accepted Manuscripts are published online shortly after acceptance, before technical editing, formatting and proof reading. Using this free service, authors can make their results available to the community, in citable form, before we publish the edited article. We will replace this Accepted Manuscript with the edited and formatted Advance Article as soon as it is available.

You can find more information about Accepted Manuscripts in the Information for Authors.

Please note that technical editing may introduce minor changes to the text and/or graphics, which may alter content. The journal's standard Terms & Conditions and the Ethical guidelines still apply. In no event shall the Royal Society of Chemistry be held responsible for any errors or omissions in this Accepted Manuscript or any consequences arising from the use of any information it contains.

ROYAL SOCIETY
OF CHEMISTRY

rsc.li/materials-a

View Article Online
DOI: 10.1039/D2TA02918A

Visualization and monitoring of dynamic damaging-healing processes of polymers by AIEgen-loaded multifunctional microcapsules

Received 00th January 20xx,
Accepted 00th January 20xx

DOI: 10.1039/x0xx00000x

Shusheng Chen,[abcd] Ting Han,*[a] Junkai Liu,[e] Xinting Liang,[f] Jinglei Yang*[bc] and Ben Zhong Tang*[eg]

The sensitive detection and dynamic monitoring of structural health of polymers is crucial to increase their quality, reliability, and durability. Although great efforts have been devoted to the indication of static damaged and/or healed states of polymers, the simple, sensitive, and real-time monitoring of dynamic damaging-healing processes still remains challenging. In this work, a facile design strategy for multifunctional polymer coatings that can sensitively show their damaging-healing processes in an on-site, real-time, and full-field manner is demonstrated. By embedding UV-blocking microcapsules containing the diisocyanate solution of aggregation-induced emission luminogen (AIEgen) into a polymer matrix, immediate turn-on fluorescence is observed upon damaging, and dual-signal variations in both fluorescence intensity and color can be clearly visualized during the dynamic healing process. These changes can also be readily and semi-quantitatively detected by fluorescence spectrometer and digital image correlation analysis. Such a high-contrast fluorescence change is achieved due to the collective effects of AIE and twisted intramolecular charge transfer of the luminogen. Benefiting from the multifunctional microcapsules, the composite polymeric coatings exhibit excellent photo-protective and water-proof performance in addition to the autonomous damaging-healing visualization capability, which are appealing to various practical applications.

Introduction

Polymers are everywhere in our daily life and play an indispensable role in the development of modern society. They are widely used as structural materials or functional coatings in housewares, biomedical supplies, aerospace industry, marine transportation, electronic packaging, etc. Polymers are required to be as robust as possible for most engineering applications. However, damage, especially small-scale cracks that results from manufacture processes or environmental stress during usage, is inevitable.[1] The occurrence and propagation of such small-scale damage can cause the compromise of structural integrality of polymers and eventually lead to catastrophic failure in materials performance. For example, in marine industries, the corrosion resistance of polymeric coatings will be greatly compromised once micro- or mesoscopic cracks occur, consequently causing significant environmental and economic losses.[2] Microcracks in functional polymer coatings for the packaging of precise electronics are harmful for their protection properties such as vacuum sealing, water-proof and lightproof performances, ultimately resulting in the performance failure of the electronic products.[3] Therefore, to improve the quality, reliability, and durability of critical polymeric components, it is crucial to sensitively detect and dynamically monitor the structural health of polymers during use.[4, 5]

Conventional techniques for evaluating the structural health of polymers usually rely on electron microscopies, such as scanning electron microscopy and transmission electron microscopy.[6, 7] Although these techniques have been widely used, their sample preparation procedures are often troublesome and may cause an irreversible change in the sample structure. In some cases, non-destructive methods including infrared imaging, radiography, and ultrasonic imaging are utilized to detect the health states of structural polymers.[8] However, these methods are generally time-consuming and require well-trained technicians to operate the high-cost instruments and analyze the indirect output signals or curves. Most importantly, these methods are not suitable for the in-situ

---

[a] Center for AIE Research, Shenzhen Key Laboratory of Polymer Science and Technology, Guangdong Research Center for Interfacial Engineering of Functional Materials, College of Materials Science and Engineering, Shenzhen University, Shenzhen 518060, China. E-mail: hanting@szu.edu.cn
[b] Department of Mechanical and Aerospace Engineering, The Hong Kong University of Science and Technology, Clear Water Bay, Hong Kong SAR, China. E-mail: maeyang@ust.hk
[c] HKUST Shenzhen-Hong Kong Collaborative Innovation Research Institute, Futian, Shenzhen 518048, China
[d] School of Chemistry and Environmental Engineering, Hanshan Normal University, Chaozhou, Guangdong 521041, China
[e] Department of Chemistry, Hong Kong Branch of Chinese National Engineering Research Center for Tissue Restoration and Reconstruction, The Hong Kong University of Science and Technology, Clear Water Bay, Kowloon, Hong Kong, China
[f] Key Laboratory of Bioorganic Chemistry and Molecular Engineering of Ministry of Education and Beijing National Laboratory for Molecular Science, and Peking-Tsinghua Center for Life Sciences, Peking University, Beijing 100871, China.
[g] School of Science and Engineering, Shenzhen Institute of Aggregate Science and Technology, The Chinese University of Hong Kong, Shenzhen, Guangdong 518172, China. E-mail: tangbenz@cuhk.edu.cn

Electronic Supplementary Information (ESI) available. See DOI: 10.1039/x0xx00000xz and real-time detection and monitoring of the structure health of polymers during use.[9] For smart polymer composites with self-healing capability, their static healing degree and dynamic healing processes are also difficult to be sensitively and directly visualized through traditional characterization methods. As seeing is believing, the development of simple and direct methods that can achieve real-time, on-site, full-field, and sensitive visualization and monitoring of damaging-healing processes of polymers is thus highly desirable in both academia and industry.

To achieve this goal, fluorescence-based methods are the most promising candidates due to their advantages of visible and portable detection, fast response, non-invasiveness, high sensitivity, and large contrast.[10-14] Nevertheless, conventional fluorophores often suffer from low fluorescence efficiencies in condensed states and poor photobleaching resistance due to the aggregation-caused quenching effect,[15] which greatly hinder their applications as optical indicators for the real-time monitoring of dynamic processes in solid polymeric materials. Fortunately, aggregation-induced emission luminogens (AIEgens) provide a good solution to this problem.[16-21] AIEgens show weak or no fluorescence in solutions but become highly emissive upon aggregation. The bright solid-state fluorescence and excellent photostability of AIEgens as well as their sensitive response to microenvironment variation enable them to serve as ideal optical indicators to visualize both static health states and dynamic processes with low background noise. Attracted by the advantages of AIEgens, great efforts have been devoted to applying AIEgens for the damage visualization in polymers.[22, 23] However, previous work mainly focused on the indication of static damaged and/or final healed states of polymers by AIEgens using either fluorescence intensity or fluorescence color as the output.[24-30] The real-time, full-field and semi-quantitative monitoring of dynamic damaging-healing processes based on the more accurate dual signal output of brightness and color of AIEgens has been less reported. Besides, the existing examples of the dual detection of crack and healed states of polymer coatings generally relied on the combination of AIEgen and UV-induced healing systems,[27-29] which are too complicated for practical applications, and the mechanistic insights need to be further investigated to provide a clearer design guideline.

Herein, we aim to develop simple yet multifunctional polymer coatings that can visually and sensitively monitor their dynamic damaging-healing processes of polymers through the dual signal variation of fluorescence brightness and color of single-component microcapsules (MCs). The dual-signal indication could greatly improve the sensitivity and accuracy of the process visualization. Instead of modifying coating structures, novel MCs with UV-blocking shells will be prepared, which not only can enhance the sensitivity and contrast of detection but also can provide photoprotection for the sensitive core. The incorporation of such UV-blocking MCs into polymer matrices could provide the corresponding coatings with additional photoprotection and potential water-proof capabilities.

Results and Discussion

View Article Online
DOI: 10.1039/D2TA02918A

To achieve the dual-signal indication, we first propose a possible design concept based on the working mechanism of AIEgen with a twisted intramolecular charge transfer (TICT) effect (referred as TICT-type AIEgen).[31-33] As schematically illustrated in Fig. 1a, owing to the twisted donor (D)-acceptor (A) structures, both the fluorescence intensity and fluorescence color of TICT-type AIEgen show sensitive response to their surrounding microenvironments such as rigidity and polarity.[34-36] TICT-type AIEgen is capable of showing obvious fluorescence in solvents with suitable polarity. With an increase in the restriction effect or a decrease in the polarity of microenvironments, the TICT-type AIEgen would show an obvious blueshift in the emission color accompanied with remarkably enhanced emission intensity due to the collective influences of TICT and restriction of intramolecular motions (RIM). In the free or polar environments such as in relatively polar solvents, the TICT-type AIEgen will be in the TICT state with its D and A units existing in a twisted conformation. The total charge separation of TICT state leads to a relatively narrower bandgap than the locally excited (LE) state. When the intramolecular motions of TICT-type AIEgen are restricted by solidification, its fluorescence intensity will be gradually enhanced due to the AIE effect. Meanwhile, the D and A units might adopt an almost parallel arrangement in the excited state to show the LE-state fluorescence with a blue-shifted emission wavelength.

Taking advantage of this unique characteristic of TICT-type AIEgen, a facile design to visualize the entire damaging-healing processes of MC-based self-healing polymers is illustrated in Fig. 1b. Diisocyanate, which automatically reacts with moisture, is an ideal liquid core that can function as both the solvent of TICT-type AIEgen and the inherent healing agent.[37, 38] The diisocyanate solution of a TICT-type AIEgen is first encapsulated by novel UV-blocking shells to form robust and potentially UV-blocking MCs. Then the AIEgen-loaded functional MCs will be dispersed in polymer matrix. When the MC-embedded polymer coating is damaged, the broken MCs will release the diisocyanate solution of TICT-type AIEgen into the cracks to show obvious fluorescence in the damaged regions. Meanwhile, the released diisocyanate will gradually change from liquid state to solid state because of its spontaneous reaction with moisture in air. During this healing polymerization, the damaged regions are expected to exhibit blue-shifted emission color and increased emission intensity due to the increasing restriction of the TICT-type AIEgen. In this sense, both the static health states and the whole damaging-healing processes of the MC-based autonomous polymer coatings will be facilely and directly visualized by the dual-signal indication in an in-situ and real-time manner. Combined with the potential light blocking properties of the MCs, the MC-embedded polymer composites could be developed as multifunctional coating materials.

To verify the feasibility of the design principle, three TICT-type AIEgens with typical D-π-A structures named as DMTPE-BMO, TPA-BMO, and TPE-BMO were utilized as fluorescent molecular rotors (Fig. 2a). In these luminogens, the dimethoxyl-tetraphenylethene (DMTPE), triphenylamine (TPA), and

View Article Online
DOI: 10.1039/D2TA02918A

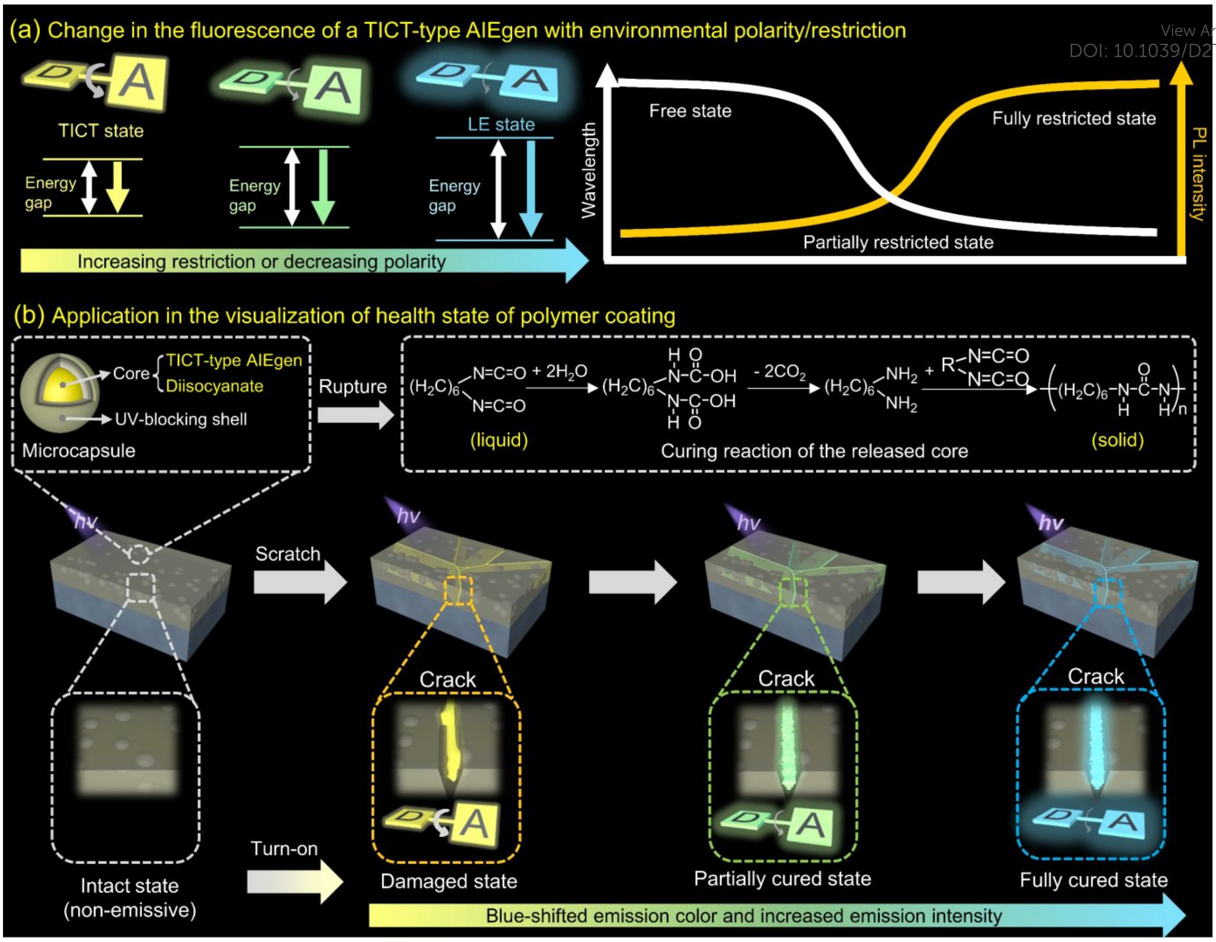

Fig. 1 Schematic illustration of the design principle. (a) Fluorescence change of TICT-type AIEgen with environmental polarity/restriction and (b) Working mechanism of microcapsules containing TICT-type AIEgen and isocyanate for the visualization of health states of polymer coatings.

tetraphenylethene (TPE) moiety are electron donors, while the BMO ((*Z*)-4-benzylidene-2-methyloxazol-5(4*H*)-one) unit serves as the π-bridge and electron acceptor. This group of TICT-type AIEgens have been proved to be greatly sensitive to environmental changes such as polarity and rigidity.[21, 39, 40] The absorption spectra of HDI solutions of these TICT-type AIEgens are similar to those of their THF solutions, showing the maximum absorption wavelength at 390 nm for DMTPE-BMO, 410 nm for TPA-BMO, and 375 nm for TPE-BMO (Fig. S1). The fluorescence properties of the HDI solutions of TICT-type AIEgens before and after reaction with water to form polyurea (PU) solid were measured by the photoluminescence (PL) and the fluorescence quantum yields (Φ_F). As shown in Fig. 2b and Fig. S2a, DMTPE-BMO exhibits a remarkable hypsochromic shift from orange emission with a maximum emission wavelength (λ_{max}) of 602 nm in HDI solution state to yellowish-green emission (λ_{max} = 531 nm) in PU solid state due to its TICT characteristic. Although DMTPE-BMO exhibits strong fluorescence in PU (Φ_F = 46%) because of the RIM effect, the emission intensity of its HDI solution is too weak to be distinguished (Φ_F = 2%). Like DMTPE-BMO, the fluorescence of TPA-BMO shows a 64-nm blueshift from HDI to PU (Fig. 2c and Fig. S2b). However, the emission intensity of TPA-BMO in the solution state (Φ_F = 68%) is similar to its PU state (Φ_F = 70%). This could be explained by the fewer rotor moieties of TPA-BMO than that of DMTPE-BMO because the change in emission intensity of fluorophores is considered to be mainly affected by intramolecular rotations. In terms of TPE-BMO, it exhibits not only a remarkable blueshift in λ_{max} from 556 nm (HDI) to 473 nm (PU) but also a sharp increase in fluorescent intensity with the Φ_F increasing from 11% (HDI) to 62% (PU) (Fig. 2d and Fig. S2c). Moreover, the fluorescence of the HDI solution of TPE-BMO can be readily detected by both fluorescence spectrophotometer and the naked eye. Considering the desired dual fluorescence signal change of the HDI solution of TPE-BMO in response to the curing reaction, TPE-BMO was selected as the model optical indicator for the following study.

To investigate the role of curing reaction on fluorescence variation, we first monitored the time-dependent PL spectra for the whole reaction process of HDI and water at 60 °C using fluorescence spectrophotometer. Fig. 2e shows that the emission spectrum of the TPE-BMO/HDI solution exhibits a first slight redshift followed by a remarkable blueshift as the reaction time goes on. The emission intensity decreases slightly at the beginning of the reaction and then increases dramatically from around 272 min to the end of the curing process (Fig. 2f and Fig. S3). The λ_{max} and maximum emission intensity were plotted as a function of time for easy comparison (Fig. 2g). As mentioned before, TICT-type AIEgens are highly sensitive to the variation in surrounding microenvironments, such as steric

View Article Online
DOI: 10.1039/D2TA02918A

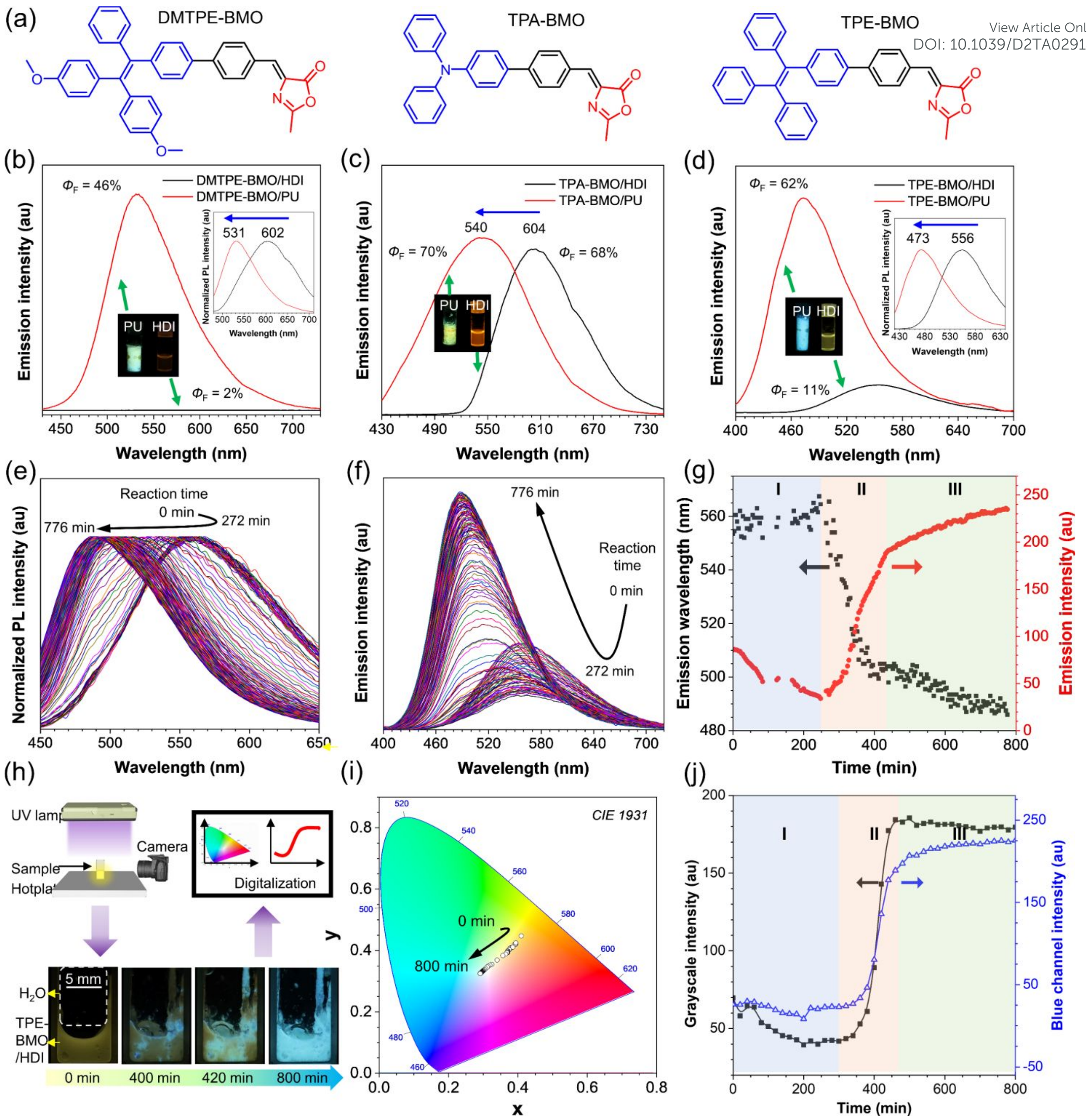

Fig. 2 (a) Chemical structures of the selected TICT-type AIEgens. (b-d) PL spectra and fluorescence quantum yields (Φ_F) of (b) DMTPE-BMO, (c) TPA-BMO, (d) TPE-BMO in HDI solutions and PU solids. Excitation wavelength: 390 nm for DMTPE-BMO; 410 nm for TPA-BMO; 375 nm for TPE-BMO. Insets are normalized PL spectra and fluorescence images of the specimens taken under 365 nm UV light illumination. (e and f) Time-dependent PL spectra of the TPE-BMO/HDI solution during curing reaction with water. (g) Plots of the maximum emission wavelength and emission intensity as a function of time for the TPE-BMO/HDI solution during its curing reaction with water. (h) Schematic illustration of the experimental setup for fluorescence imaging of the TPE-BMO/HDI solution during curing reaction with water, and time-dependent fluorescence images of the TPE-BMO/HDI solution during curing reaction with water taken under 365 nm UV light illumination. (i) CIE coordinates on the CIE 1931 chromaticity diagram and (j) grayscale intensity as a function of time for the fluorescence images of the TPE-BMO/HDI solution during curing reaction with water.

restriction, polarity, and D-A efficacy and strength.[34, 35, 41] Therefore, the observed variation tendency in fluorescence behaviors may arise from the competitive influence of viscosity, restriction, polarity, and temperature. Increasing viscosity or restriction is favorable for blue-shifting and enhancing the light emission, whereas the increase in microenvironment polarity and temperature tends to result in red-shifted and decreased fluorescence.

In the initial stage (stage I), the increase in the viscosity of the reaction system should be very slow according to the step-growth polymerization mechanism, which allows TPE-BMO to possess good flexibility in this sol state [42-44]. Meanwhile, the microenvironment polarity might increase due to the formation

View Article Online
DOI: 10.1039/D2TA02916A

of polar units, such as -NHCOOH and -NH_2, during the induction period of the reaction between –NCO groups and water (Fig. 1b). Besides, the heating process (Fig. S4) and the exothermal effect of this curing reaction at this stage could also weaken and redshift the fluorescence of the mixture to some extent. Consequently, the unexpected slight redshift and decrease of fluorescence in the initial reaction stage could be explained by the leading role of microenvironment polarity and temperature variations at such circumstances. Once the crosslinking reaction occurs to transform the sol to gel state, the viscosity will increase dramatically to overwhelm the effects of polarity and temperature, thereby showing sharply increased and blue-shifted fluorescence change in stage II. In the final stage (stage III) of the curing reaction, the intramolecular motions and the conformation of TPE-BMO molecules are restricted to a large extent. The slowly increased intensity and slightly blue-shifted emission might result from slower diffusion of monomers in the highly viscous or even solid state.[45]

Encouraged by the PL results, we then explored the possibility for the direct visualization of the large-scale curing process of TPE-BMO/HDI and water based on digital image correlation (DIC). A homemade imaging system that consists of a UV lamp controlled by a smartphone, a camera with a self-timer, and a computer program was built as shown in Fig. 2h and Fig. S5. The fluorescence photos of the sample can be taken automatically and transferred to digital information, such as CIE color space, grayscale, and RGB channel intensity, by using this simple imaging system. The sample to be observed, namely a cuvette with water in the top layer and TPE-BMO/HDI in the bottom layer, was placed under the UV lamp. To accelerate the curing reaction, the experiment was conducted at 60 ^{o}C. The change in fluorescence was monitored by controllably taking photos at different time and the post-processing of a series of digital photographs. This measurement setup provides a simple, real-time, on-site, and continuous DIC method for the tracking of the curing process. Fig. 2h and Fig. S6 depict the real-time fluorescence images obtained during the curing process. These fluorescence images not only show the overall curing process in a full field of view, but also indicate whether, when, and where the curing reaction occurs. The transition from liquid state to solid state observed in these digital images further supports our abovementioned explanation for the time-dependent fluorescence change. Furthermore, a computer MATLAB digitalization program was utilized to transform the fluorescence images to the average CIE color space, grayscale, and RGB channel intensity. The color chromaticity chart in Fig. 2i shows that the fluorescence color changes from yellow to blue with reaction time. The blue channel intensity exhibits the biggest change compared with the green and red channel intensities (Fig. S7), indicating an apparent blueshift. The time-dependent grayscale curve suggests that the emission intensity sequentially experiences a slight decline, a sharp increase, and an almost stable stage during the curing process (Fig. 2j). The results obtained by the facile DIC method are nearly consistent with the PL results.

To reveal the underlying working mechanism and meanwhile to verify our design principle from the mechanistic point of view, we then carried out the associated comparative experiments and theoretical calculations. Firstly, the PL spectrum of TPE-BMO/HDI solution was measured at 77 K to investigate the effect of rigidification on the fluorescence of TPE-BMO. As shown in Fig. 3a, upon cooling the solution from 298 K to 77 K, the relatively weak yellow emission of the TPE-BMO/HDI solution remarkably changes to bright blue emission with a 74-nm blueshift in λ_{max}. Nevertheless, the transition from HDI solution to PU solid at room temperature leads to an even more obvious blueshift of 83 nm in the λ_{max} of TPE-BMO. This experimental result suggests the synergistic effects of the rigidity and polarity of solid PU on the fluorescence behaviors of TPE-BMO [46], where the restriction effect might play a dominant role in fluorescence change. To gain further insight into the synergistic effects, the oscillator strength of S_1 of TPE-BMO as a function of dihedral angles was calculated (Fig. 3b and 3c). The results show that the oscillator strength decreases with an increase in dihedral angles. The lower is the oscillator strength, the weaker fluorescence the luminogen will show.[47] We then calculated the optimum conformation of TPE-BMO in hexane, tetrahydrofuran (THF), and crystal state. Among them, TPE-BMO/THF was used to simulate TPE-BMO/HDI due to the similar polarity of these two solvents.[48] The environmental polarity reduces from THF to hexane, while the restriction effect increases from THF state to crystal state. Fig. S8 shows that the dihedral angle of TPE-BMO around the C3=C4 double bond becomes smaller when the environment polarity decreases or the restriction effect increases, thus leading to the recovery of the locally excited state with higher oscillator strength in low polarity and highly emissive state with low nonradiative decay in the crystal. In this sense, the variation in fluorescence intensity from TPE-BMO/HDI to TPE-BMO/PU may be due to effects of the restriction increment and/or the polarity decline from HDI solution to PU solids. The highest occupied molecular orbital (HOMO) and the lowest unoccupied molecular orbital (LUMO) results of TPE-BMO in three states are provided in Fig. 3d. The bandgap becomes wider with a decrease in polarity or an increase in restriction, which causes a hypsochromic shift in the emission spectrum. This calculation result suggests that the dramatically blue-shifted fluorescence of TPE-BMO in PU solids could result from the collective effects of the decreased polarity and the increased rigidity.

Based on the sensitive fluorescence response of TPE-BMO to microenvironment variations, we then tried to prepare the desired MCs and MC-embedded polymers to demonstrate the concept shown in Fig. 1b. Novel MCs composed of UV-blocking shells and the TPE-BMO/HDI liquid core were prepared via a multi-step method. As depicted in Fig. 4a, this method involved an interfacial polymerization followed by the repeated dopamine self-polymerization. Detailed preparation procedures can be found in the supporting information. The formation of four polydopamine (PDA) layers aims to improve the UV-shielding ability of MCs,[49-52] thereby increasing the fluorescence contrast of intact and broken MCs. The resulting MCs of each step were denoted as PU MCs, 1PDA/PU MCs, 2PDA/PU MCs, 3PDA/PU MCs, and 4PDA/PU MCs according to the layer composition. The SEM imaging results in Fig. 4b

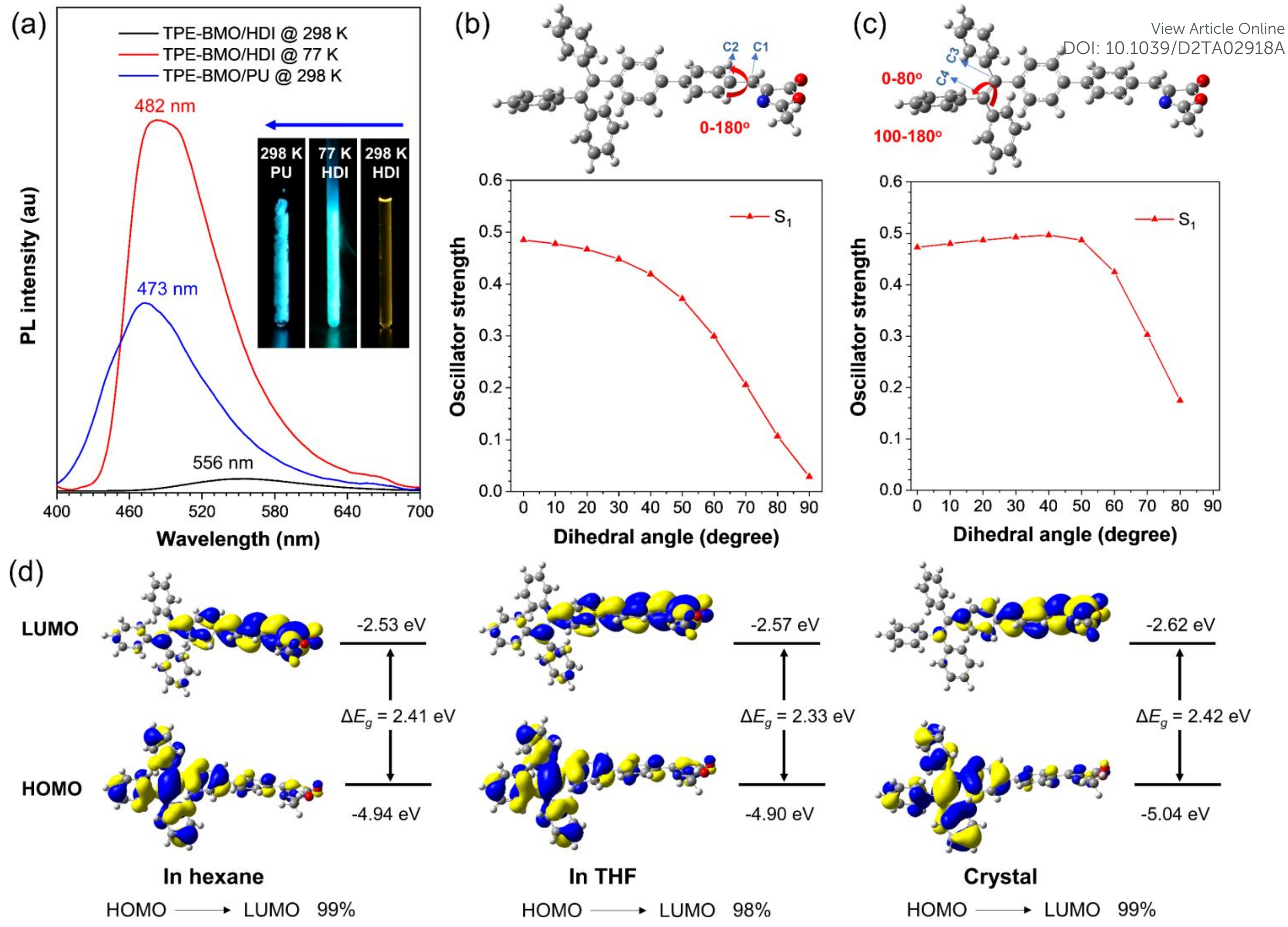

Fig. 3 (a) PL spectra of TPE-BMO/HDI solutions at room temperature (298 K) and 77 K, and TPE-BMO/PU solid at room temperature (298 K). Potential energy profiles of S_1 and S_0 with (b) rotating of C1-C2 single bond and (c) rotating of C3=C4 double bond of TPE-BMO (dihedral angle: 0-180°) in gas calculated at TD-B3LYP/6-31G(d,p) level. (d) Molecular orbitals of TPE-BMO in gas, THF (simulation for HDI), and crystal state in the transition from S_0 to S_1 calculated at TD-B3LYP/6-31G(d,p) level.

suggest that the 4PDA/PU MCs possess nearly spherical morphologies, and a core-shell structure can be clearly observed. The outer surface of the MCs is rough and deposited with many small particles of PDA. Conversely, the PU MCs are too weak to keep the steric structures under a high vacuum during SEM imaging, and their outer surfaces are smooth without PDA layers (Fig. S9). The composition and mechanical properties of the MCs were also characterized. As shown in Figure S10, the characteristic absorption peak of the –NCO group at about 2270 cm^{-1} can be observed in the IR spectra of HDI, PU MCs and 4PDA/PU MCs, indicating the successful encapsulation of HDI. The core fraction of 4PDA/PU MCs was calculated to be around 65% according to the TGA curves, suggesting the good encapsulation efficiency of our method (Figure S11). The mechanical properties of MCs were evaluated by quasi-static compression at a single-capsule level. As depicted in Figure S12, the presence of PDA layers can remarkably improve the mechanical strength of the MCs compared with that of the PU MCs. Moreover, with an increase in the number of PDA layers, the nominal strength of the MCs can grow from 117 ± 11 KPa (1PDA/PU MCs) to 343 ± 49 KPa (4PDA/PU MCs).

The presence of PDA shells makes the appearance color of the MCs change from yellow to black under room light, and the bright yellow fluorescence from the PU MCs can be blocked to different extent (Fig. S13). To quantitatively compare the UV-shielding capability of these multi-layered MCs, a fluorescence microscope was used to detect the fluorescence of individual MCs and measure the grayscale intensity of the fluorescence images. As shown in Fig. 4c, the fluorescence brightness of individual MCs gradually decreases from PU MCs to 4PDA/PU MCs under UV illumination. The corresponding grayscale value dramatically reduces from around 200 for PU MCs to 2 for 4PDA/PU MCs. These results clearly verify the excellent light-shielding ability of the 4PDA/PU shell. The fluorescence from the TPE-BMO-containing core can be almost completely blocked after depositing four PDA layers on the MC surface. Therefore, 4PDA/PU MCs were used for the following investigation.

To evaluate the tracking ability of 4PDA/PU MCs containing the HDI solution of TPE-BMO (TPE-BMO/HDI MCs) for the damaging-healing process, a few intact and damaged MCs were simultaneously spread on a glass slide and observed under a fluorescence microscope. As shown in Fig. 4d, the intact MCs are non-emissive, whereas the damaged MCs emit yellow

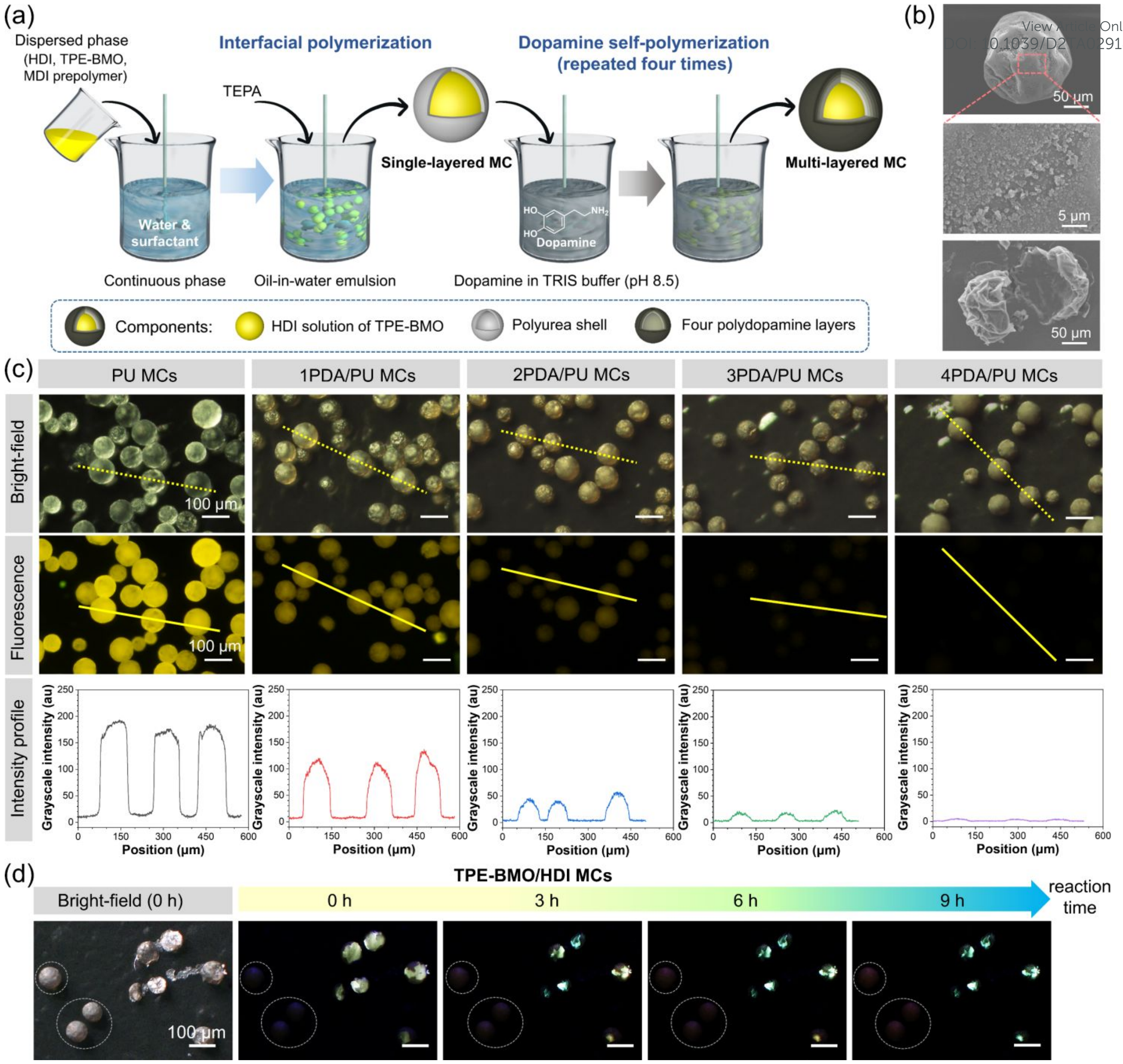

Fig. 4 (a) Schematic illustration of the preparation procedures of the UV-blocking microcapsules (MCs) containing the HDI solution of TPE-BMO. (b) SEM images of 4PDA/PU MCs: an individual MC, the enlarged-outer surface, and a ruptured MC. (c) Micrographs (upper and middle panels) and the associated grayscale intensity profiles (bottom panel) of PU MCs, 1PDA/PU MCs, 2PDA/PU MCs, 3PDA/PU MCs, and 4PDA/PU MCs taken under bright field (upper panel) and the illumination of light with an excitation wavelength of 460–490 nm (middle panel). The grayscale intensity profiles correspond to the line areas in the fluorescence micrographs. (d) Micrographs of 4PDA/PU microcapsules containing the HDI solution of TPE-BMO (TPE-BMO/HDI MCs) taken under bright field and 365 nm UV light illumination at different reaction time during the healing process.

fluorescence at the beginning. The emission color gradually blue-shifts with reaction time. Apart from the blueshift of fluorescence, an increase in the emission intensity was also observed, which indicates the potential of TPE-BMO/HDI MCs for the visualization of the damage-healing process with dual-fluorescence signals.

To investigate the visualization application of 4PDA/PU MCs in polymer coatings, MCs with diameters of 140 ± 37 μm (Fig. S14) were embedded into epoxy (EP) matrix by casting in a cylindrical vessel and then demoulding. As presented in Fig. 5a and Fig. S15, no fluorescence can be observed for the intact specimen under UV illumination. Upon being manually scratched, the injured regions can be readily indicated by the immediate occurrence of bright yellow luminescence. By contrast, it is difficult to distinguish the damaged areas of the sample under room light. This result confirms the powerful damage-reporting capability of the fluorescence-based sensing technique. As the reaction time increases, the evolution of the entire healing process can be clearly monitored in a large field of view by an obvious variation in both the fluorescence color and intensity. Moreover, accidental and minor damage (inside the gray frames of Fig. 5a) of the EP plate that is hard to observe at the very beginning can also be repaired and obviously indicated after the self-healing process. It is worth noting that

View Article Online
DOI: 10.1039/D2TA02918A

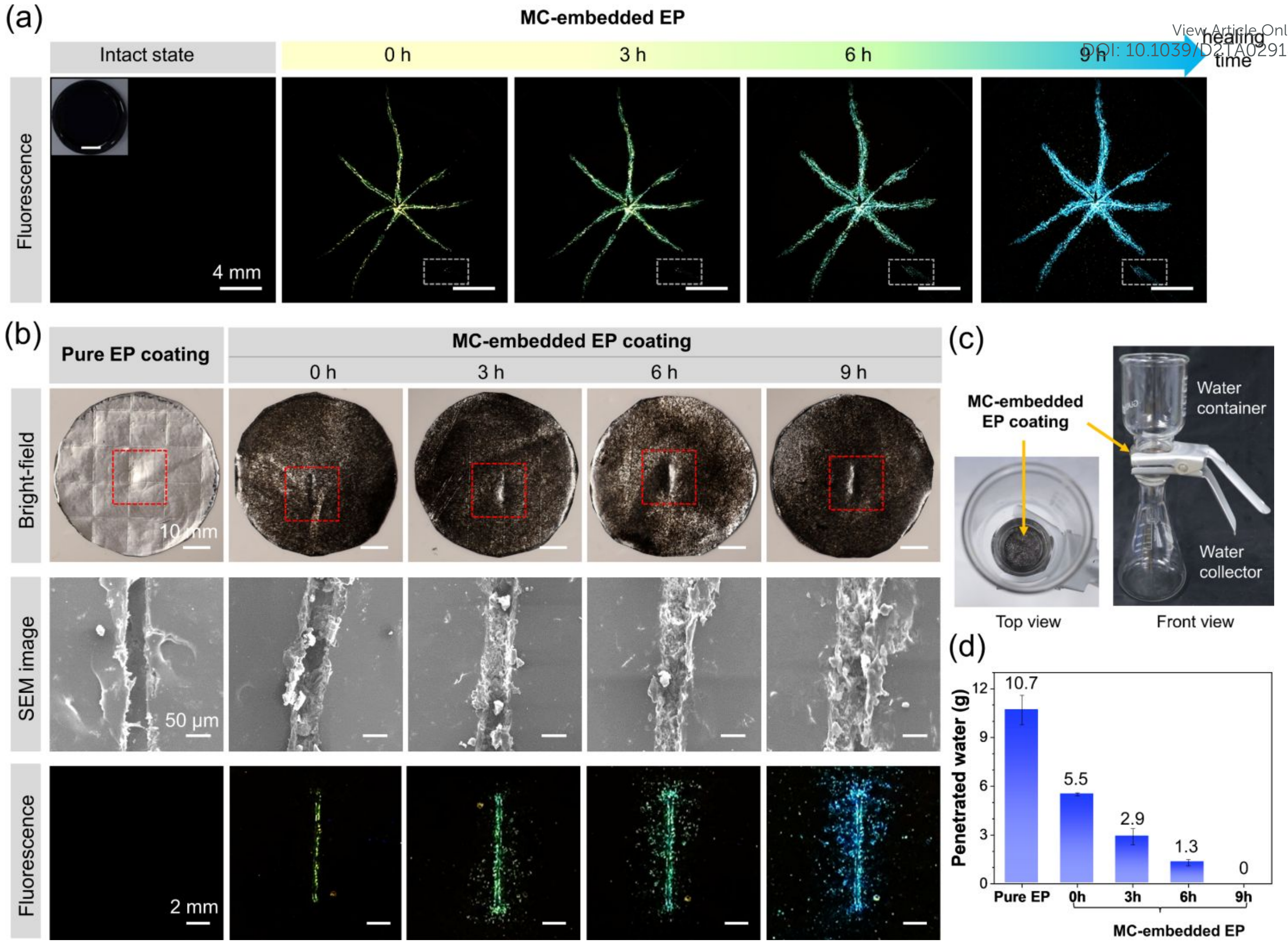

Fig. 5 (a) Fluorescent images of the MC-embedded epoxy (EP) coating in the intact state and damaged state at different healing time. The inset is the whole photograph of the intact EP coating taken under room light (scale bar = 8 mm). (b) Bright-field photographs, SEM images, and fluorescence images of a pure EP coating and the MC-embedded EP coatings at different healing time. (c) Experimental setup of water permeation test. (d) The water-permeation capability of the cracked pure EP coating and MC-embedded EP coatings at different healing time.

no emission is observed from intact MCs during the whole observation period, suggesting the excellent stability of the MCs as well as the high contrast and low background noise of this visualization method. In addition, the fluorescence intensity of these fluorescence images can be transformed to grayscale by the facile DIC method using MATLAB program, and the whole EP sample can be mapped with a color bar ranging from blue to red (Fig. S16). All these results demonstrate that the proposed method is promising for use in the direct, real-time, on-site, full-field, and sensitive visualization and monitoring of dynamic damaging-healing processes of polymers.

A correlation between our fluorescence-based sensing method and the traditional self-healing characterization techniques was also investigated. As depicted in Fig. 5b, a pure EP coating and the MC-embedded EP coatings were coated on aluminized paper, respectively, and narrow through-thickness cracks were created with a sharp blade. The cracks of the MC-embedded EP coatings initially show weak yellow emission and then gradually emit bright-blue fluorescence over time, whereas no signal can be detected from the pure EP coating. The SEM images reveal that the cracks of MC-embedded EP coatings are partially sealed without sufficient healing time such as at 3h and 6 h. After healing for 9 h, the cracks are completely filled by the newly formed materials. These results are consistent with the variation in fluorescence signals. Compared with the SEM technique, our method possesses the on-site and full-field advantages for a complicated real sample. To semi-quantitatively check the health state of the cracked polymer coatings, a water permeation test was performed using an experiment setup shown in Fig. 5c,[53] and the results in Fig. 5d shows that the pure EP coating undergoes severe water permeation, whereas the MC-embedded EP coatings possess water-proof function. The average weight of permeated water decreases from 5.5 g for the unhealed sample to 2.9 g and 1.3 g for the partially healed ones. No water permeation can be observed for the fully healed specimen. This result indicates that the fluorescence signals of the MC-embedded coatings can be directly correlated to their health states such as the water-proof degree.

Taking advantage of the light-shielding ability of the MC shell, we further investigated the photoprotection property of the MC-embedded EP coating. As shown in Fig. 6a, due to the Tyndall effect, a light path from a red laser pointer pen can be clearly observed in a bottle of silica sol without the polymer coating. In sharp contrast, the Tyndall phenomenon disappears after placing an MC-embedded EP coating in front of the silica

View Article Online
DOI: 10.1039/D2TA02918A

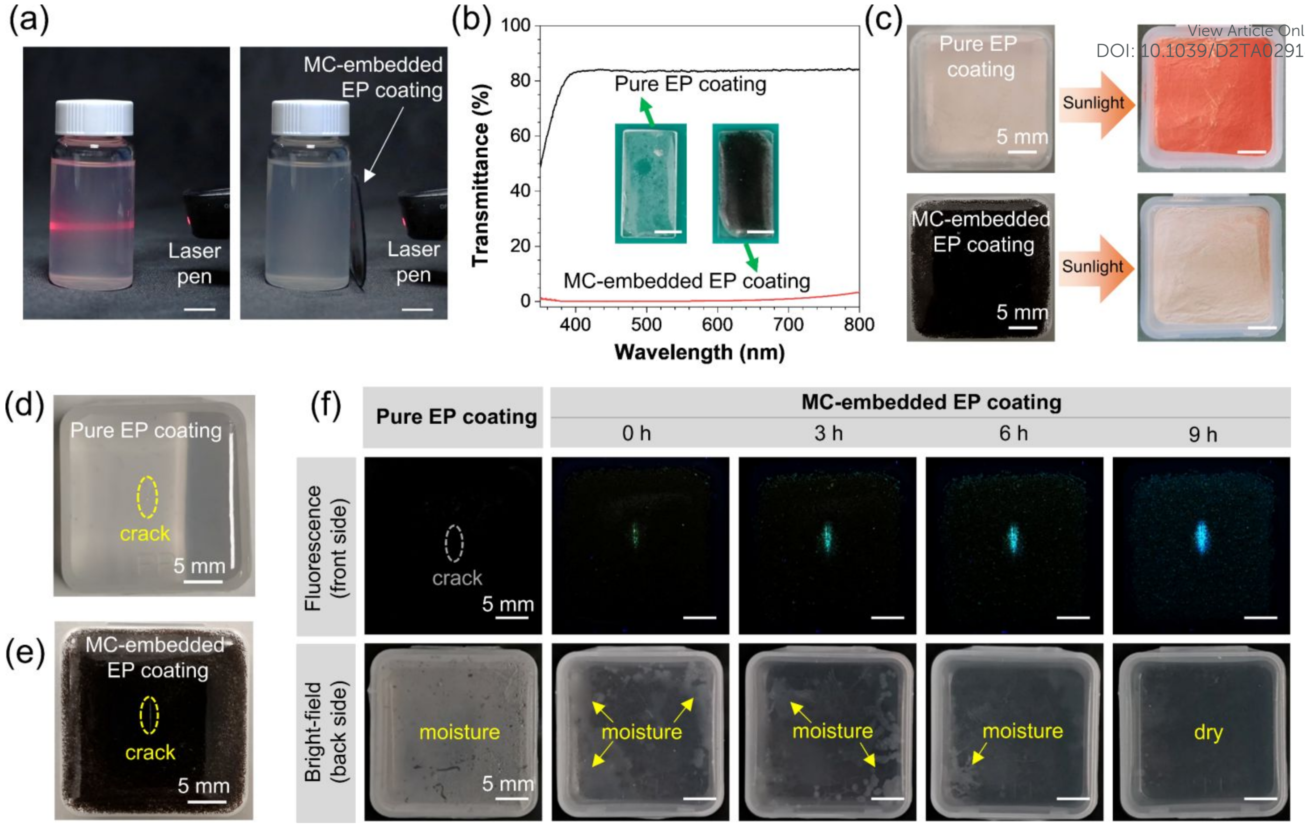

Fig. 6 (a) The Tyndall effect in a bottle of silica sol without and with an MC-embedded EP. The scale bar indicates 2 mm. (b) UV-Vis transmittance spectra and the associated photographs of quartz glass plates coated with a pure EP coating and an MC-embedded EP coating, respectively. The scale bar in the insets indicates 5 mm. (c) Photographs showing the front sides of boxes coated with pure EP and MC-embedded EP, and their inside photosensitive powders before and after placing under sunlight for 5 min. (d and e) Photographs showing the front side of a cracked box coated with (d) pure EP coating and (e) MC-embedded EP coating taken under room light. (f) Fluorescence images showing front sides of cracked boxes coated with pure EP coating or MC-embedded EP coatings at different healing time (upper panel). Bright-field photographs showing back sides of cracked boxes with pure EP coating and MC-embedded EP coating at different healing time after evaporating the penetrated water inside (lower panel).

sol. The optical transmittance of the MC-embedded EP coating on quartz glass was also measured and compared with that of a pure EP coating. As depicted in Fig. 6b, the pure EP coating exhibits high transmittances of about 84% in the visible light region (400–800 nm) and above 50% in the UV light region of 350–400 nm. By comparison, the MC-embedded EP coating shows transmittances of lower than 3% for the whole testing wavelength range. These results convincingly demonstrate the excellent photoprotection performance of the MC-embedded coating. Considering the autonomous damage-healing indication capability, excellent UV-vis light-shielding property, as well as the direct and sensitive visualization of the level of water-proofing, of the MC-embedded EP composites are promising to serve as multifunctional coating materials in packaging applications for the storage of photo- and/or water-sensitive objects, such as photoresist, photosensitizers, and electronic memory chips.

To demonstrate the applicability of such EP coatings, we then conducted a proof-of-concept study. As depicted in Fig. 6c, a pure EP coating and a MC-embedded EP were applied to the front side of thin plastic boxes. containing photosensitive powders. After placing the boxes under sunlight illumination for 5 min, the color of the photosensitive powders in the pure EP-coated box remarkably changes from white to orange, while those in the box coated with MC-embedded EP keep stable with little color change. In addition to the photoprotection function, the damage-warning, health indication, self-healing, and water-proof functionalities of such coatings were also demonstrated. As shown in Fig. 6d-f, when narrow through-thickness cracks were caused to the coatings, these cracks were hardly observed under room light or in pure EP coating but can be sensitively indicated in the MC-embedded EP coating under UV light illumination. After immersing the coated boxes underwater and then placing them on a hotplate to evaporate the inside permeated water, lots of moisture was observed from the back side of the EP-coated box (lower panel of Fig. 6f). In contrast, the boxes coated with MC-embedded EP coatings exhibit less or even no moisture inside due to the reaction of the released HDI with water. Moreover, the whole healing process can be readily monitored by the dual-fluorescence variations. In other words, users can evaluate the health state or the water-proof performance of the functional coatings simply by fluorescence signals in a real-time, on-site, and quantifiable manner. In this regard, this method can help the related users to take necessary actions before the malfunction or failure occurs. Overall, the MC-embedded EP coating can protect the photosensitive components, retard the water permeation through the damaged containers, and visually assess the water-proof degree, all of which are desirable functionalities for practical packaging applications.

Conclusions

In conclusion, this work demonstrated a simple yet powerful design strategy for multifunctional polymer coatings that can on-site, real-time, full-field, sensitively, visually and semi-quantitatively show their damaging-healing processes. A TICT-type AIEgen (TPE-BMO) was used as the optical indicator. Due to the collective effects of AIE and TICT, TPE-BMO exhibits dual signal changes in both fluorescence intensity and fluorescence color in response to microenvironment variations of its HDI solution. Such a sensitive fluorescence response can be detected by the naked eye, fluorescence spectrometer, and DIC analysis. By encapsulating the HDI solution of TPE-BMO inside UV-blocking shells, robust and multifunctional MCs with light-shielding and damage-healing indication capabilities were prepared. The dispersion of the AIEgen-loaded MCs in EP matrix produced polymer coatings with damage-reporting, autonomous self-healing, and health indication functionalities. Immediate turn-on fluorescence was observed upon the damage of composite coatings, and the fluorescence in the damaged areas gradually blue-shifted and became enhanced with the healing time. Furthermore, the smart polymer coatings exhibit excellent photo- and water-protective performance. Considering these attractive properties, the MC-embedded polymer composites are promising to serve as multifunctional coating materials in packaging applications. It is envisioned that such a versatile and multifunctional visualization method with a clear working mechanism can be extended to other self-healing systems and will open up new opportunities for numerous applications of smart coatings in the packaging, automobile, and shipping industries.

Author Contributions

S.C. and T.H. conceived the concepts, designed the research, and performed the experiment. J.K. performed the simulations. L.T. conducted the synthesis. S.C. and T. H. drafted the manuscript. J.Y. and B.Z.T. supervised the entire project. All authors participated in the discussion of results and revised the manuscript.

Conflicts of interest

There are no conflicts to declare.

Acknowledgements

The work was financially supported by the National Natural Science Foundation of China (Grant #: 21905176), the Project of Hetao Shenzhen-Hong Kong Science and Technology Innovation Cooperation Zone (HZQB-KCZYB-2020083), the NSFC/RGC Joint Research Scheme of Hong Kong (Grant#: N_HKUST 631/18, 51861165103), and the Science and Technology Plan of Shenzhen (JCYJ20190808142403590). The authors are grateful to Mark Ellwood from MAE of HKUST for the discussion of this work. The authors also acknowledge the Instrumental Analysis Center of Shenzhen University.

References

1. J. F. Patrick, M. J. Robb, N. R. Sottos, J. S. Moore and S. R. White, *Nature*, 2016, **540**, 363-370.
2. A. K. Leonardi and C. K. Ober, *Annu. Rev. Chem. Biomol.*, 2019, **10**, 241-264.
3. J. J. Licari, *Coating materials for electronic applications: polymers, processing, reliability, testing*, William Andrew Publishing, Norwich, NY, 2003.
4. O. Rifaie‐Graham, E. A. Apebende, L. K. Bast and N. Bruns, *Adv. Mater.*, 2018, **30**, 1705483.
5. S. McDonald, S. Coban, N. Sottos and P. Withers, *Sci. Rep.*, 2019, **9**, 1-8.
6. L. Reimer, *Ultramicroscopy*, 1984, **14**, 291-303.
7. S. Biria and I. D. Hosein, *Macromolecules*, 2017, **50**, 3617-3626.
8. S. K. Dwivedi, M. Vishwakarma and A. Soni, *Mater. Today: Proc.*, 2018, **5**, 3690-3698.
9. M. M. Caruso, D. A. Davis, Q. Shen, S. A. Odom, N. R. Sottos, S. R. White and J. S. Moore, *Chem. Rev.*, 2009, **109**, 5755-5798.
10. D. B. Lioi, V. Varshney, S. Izor, G. Neher and W. J. Kennedy, *J. Mater. Chem. C*, 2019, **7**, 14471-14492.
11. R. Kotani, H. Sotome, H. Okajima, S. Yokoyama, Y. Nakaike, A. Kashiwagi, C. Mori, Y. Nakada, S. Yamaguchi and A. Osuka, *J. Mater. Chem. C*, 2017, **5**, 5248-5256.
12. G. Postiglione, A. Colombo, C. Dragonetti, M. Levi, S. Turri and G. Griffini, *Sens. Actuators B Chem.*, 2017, **248**, 35-42.
13. X. Wang, Z. Chen, W. Xu and X. Wang, *Compos Part B-Eng*, 2020, **184**, 107744.
14. H. Feng, F. Yu, Y. Zhou, M. Li, L. Xiao and Y. Ao, *RSC Adv.*, 2020, **10**, 33675-33682.
15. J. B. Birks, *Photophysics of aromatic molecules*, Wiley, London, 1970.
16. J. Mei, N. L. Leung, R. T. Kwok, J. W. Lam and B. Z. Tang, *Chem. Rev.*, 2015, **115**, 11718-11940.
17. Z. Wang, J. Nie, W. Qin, Q. Hu and B. Z. Tang, *Nat. Commun.*, 2016, **7**, 1-8.
18. W. Wu and B. Liu, *National Science Review*, 2020, **8**.
19. Q. Li, K. Huang, Q. Qiu, X. Zhang, D. Qin and X. Zeng, *Dyes Pigm.*, 2021, 109537.
20. J. Yang, M. Fang and Z. Li, *Aggregate*, 2020, **1**, 6-18.
21. T. Han, C. Gui, J. W. Lam, M. Jiang, N. Xie, R. T. Kwok and B. Z. Tang, *Macromolecules*, 2017, **50**, 5807-5815.
22. T. Han, L. Liu, D. Wang, J. Yang and B. Z. Tang, *Macromol. Rapid Commun.*, 2021, **42**, 2000311.
23. A. Funtan, P. Michael, S. Rost, J. Omeis, K. Lienert and W. H. Binder, *Adv. Mater.*, 2021, **33**, 2100068.
24. M. J. Robb, W. Li, R. C. Gergely, C. C. Matthews, S. R. White, N. R. Sottos and J. S. Moore, *ACS Cent. Sci.*, 2016, **2**, 598-603.
25. C. Calvino, A. Guha, C. Weder and S. Schrettl, *Adv. Mater.*, 2018, **30**, 1704603.
26. X. Lu, W. Li, N. R. Sottos and J. S. Moore, *ACS Appl. Mater. Interfaces*, 2018, **10**, 40361-40365.

View Article Online
DOI: 10.1039/D2TA02918A

27. Y. K. Song, B. Kim, T. H. Lee, S. Y. Kim, J. C. Kim, S. M. Noh and Y. I. Park, *Sens. Actuators B Chem.*, 2018, **257**, 1001-1008.
28. Y. K. Song, T. H. Lee, J. C. Kim, K. C. Lee, S.-H. Lee, S. M. Noh and Y. I. Park, *Molecules*, 2019, **24**, 1679.
29. Y. K. Song, T. H. Lee, K. C. Lee, M. H. Choi, J. C. Kim, S.-H. Lee, S. M. Noh and Y. I. Park, *Appl. Surf. Sci.*, 2020, **511**, 145556.
30. S. Chen, T. Han, Y. Zhao, W. Luo, Z. Zhang, H. Su, B. Z. Tang and J. Yang, *ACS Appl. Mater. Interfaces*, 2020, **12**, 4870-4877.
31. H. Qian, M. E. Cousins, E. H. Horak, A. Wakefield, M. D. Liptak and I. Aprahamian, *Nat. Chem.*, 2017, **9**, 83-87.
32. Y. Cheng, J. Wang, Z. Qiu, X. Zheng, N. L. Leung, J. W. Lam and B. Z. Tang, *Adv. Mater.*, 2017, **29**, 1703900.
33. X. Han, F. Ge, J. Xu and X. H. Bu, *Aggregate*, 2021, **2**, e28.
34. Z. R. Grabowski, K. Rotkiewicz and W. Rettig, *Chem. Rev.*, 2003, **103**, 3899-4032.
35. S. Sasaki, G. P. Drummen and G.-i. Konishi, *J. Mater. Chem. C*, 2016, **4**, 2731-2743.
36. C. Peinado, E. Salvador, F. Catalina and A. Lozano, *Polymer*, 2001, **42**, 2815-2825.
37. J. Yang, M. W. Keller, J. S. Moore, S. R. White and N. R. Sottos, *Macromolecules*, 2008, **41**, 9650-9655.
38. M. Huang and J. Yang, *J. Mater. Chem.*, 2011, **21**, 11123-11130.
39. Y. Zhang, M. Jiang, T. Han, X. Xiao, W. Chen, L. Wang, K. S. Wong, R. Wang, K. Wang and B. Z. Tang, *ACS Appl. Mater. Interfaces*, 2018, **10**, 34418-34426.
40. M. Jiang, Z. He, Y. Zhang, H. H. Sung, J. W. Lam, Q. Peng, Y. Yan, K. S. Wong, I. D. Williams and Y. Zhao, *J. Mater. Chem. C*, 2017, **5**, 7191-7199.
41. D. Liese and G. Haberhauer, *Isr. J. Chem.*, 2018, **58**, 813-826.
42. G. Yilmaz and Y. Yagci, *Prog. Polym. Sci.*, 2020, **100**, 101178.
43. S. Ye, H. Zhang, J. Fei, C. H. Wolstenholme and X. Zhang, *Angew. Chem. Int. Ed.*, 2021, **60**, 1339-1346.
44. R. Hu, E. Lager, A. Aguilar-Aguilar, J. Liu, J. W. Lam, H. H. Sung, I. D. Williams, Y. Zhong, K. S. Wong and E. Pena-Cabrera, *J. Phys. Chem. C*, 2009, **113**, 15845-15853.
45. H. Ni, H. A. Nash, J. G. Worden and M. D. Soucek, *J. Polym. Sci., Part A: Polym. Chem.*, 2002, **40**, 1677-1688.
46. Y. Hu, L. Barbier, Z. Li, X. Ji, H. Le Blay, D. Hourdet, N. Sanson, J. W. Lam, A. Marcellan and B. Z. Tang, *Adv. Mater.*, 2021, **33**, 2101500.
47. Y. Tu, J. Liu, H. Zhang, Q. Peng, J. W. Lam and B. Z. Tang, *Angew. Chem.*, 2019, **131**, 15053-15056.
48. Y. Zhang, M. Jiang, G.-C. Han, K. Zhao, B. Z. Tang and K. S. Wong, *J. Phys. Chem. C*, 2015, **119**, 27630-27638.
49. H. Lee, S. M. Dellatore, W. M. Miller and P. B. Messersmith, *Science*, 2007, **318**, 426-430.
50. Y. Liu, K. Ai and L. Lu, *Chem. Rev.*, 2014, **114**, 5057-5115.
51. S. Chen and J. Feng, *Compos. Sci. Technol.*, 2014, **101**, 145-151.
52. S. Chen, Y. Cao and J. Feng, *ACS Appl. Mater. Interfaces*, 2014, **6**, 349-356.
53. H. Zhang, Y. B. Chong, Y. Zhao, A. Buryak and F. Duan, *Eng. Sci.*, 2019, **8**, 66-75.